

# Search for gas bulk motions in eight nearby clusters of galaxies with Suzaku

Naomi OTA<sup>1</sup> and Hiroko YOSHIDA<sup>1</sup>

<sup>1</sup>Department of Physics, Nara Women's University, Kita-uoyanishi-machi, Nara, Nara 630-8506, Japan

\*E-mail: naomi@cc.nara-wu.ac.jp

Received ; Accepted

## Abstract

To search for bulk motions of the intracluster medium, we analyzed the X-ray spectra taken with the *Suzaku* satellite and measured the Doppler shift of Fe-K line emission from eight nearby clusters of galaxies with various X-ray morphologies. In the cores of the Centaurus and Perseus clusters, the gas bulk velocity does not exceed the sound velocity, which confirms the results of previous research. For the Cen45 subcluster, we found that the radial velocity relative to the Centaurus core,  $< 780 \text{ km s}^{-1}$ , is significantly smaller than that reported in the optical band at the  $3.9\sigma$  level, which suggests an offset between the gas and galaxy distributions along the line of sight due to the subcluster merger. In A2199, A2142, A3667, and A133, no significant bulk motion was detected, indicating an upper limit on the radial velocity of  $3000 - 4000 \text{ km s}^{-1}$ . A sign of large bulk velocity in excess of the instrumental calibration uncertainty was found near the center of cool-core cluster A2029 and in the subcluster of the merging cluster A2255, suggesting that the nonthermal pressure support is not negligible in estimating the total gravitational mass of not only merging clusters but also relaxed clusters as predicted by numerical simulations. To improve the significance of the detection, however, a further examination by follow-up observations is required. The present study provides a pilot survey prior to the future high-resolution spectroscopy with *ASTRO-H*, which is expected to play a critical role in revealing the dynamical evolutions of clusters.

**Key words:** galaxies: clusters: individual (Centaurus cluster, Perseus cluster, A2029, A2199, A2142, A3667, A133, A2255) – galaxies: clusters: intracluster medium – X-rays: galaxies: clusters – cosmology: observations

## 1 Introduction

Galaxy clusters comprise the largest structures in the universe and the precise knowledge of their mass structures is important for understanding the history of structure formation and to constrain the still unknown types of dark content of the universe. The clusters are believed to have grown into their present shapes via collisions and mergers of smaller groups and clusters. If such objects collide under gravitational attraction, a huge amount of energy can possibly be released. A certain fraction of this energy is expected to heat the intracluster medium (ICM), generate nonthermal particles through shock waves, and induce

bulk and turbulent gas motions. Earlier simulations have predicted that the gas bulk motion with the speed of a substantial fraction of virial velocity ( $> 1000 \text{ km s}^{-1}$ ) will persist for several giga years (e.g., Roettiger et al. 1997; Norman & Bryan 1999; Ricker & Sarazin 2001; Dolag et al. 2005).

If the kinetic velocity of the gas is larger than its sound velocity, nonthermal pressure cannot be neglected in estimating the total gravitational mass inside the cluster. Nagai et al. (2007) used numerical simulations to show that the hydrostatic mass estimate is biased low by approximately 5–20% even in relaxed clusters. This result can be primarily attributed to an additional

pressure support provided by the bulk motions in the ICM. The departure from the hydrostatic assumption is one of the largest sources of systematic uncertainties in cluster cosmology (e.g., Lau et al. 2009; Rasia et al. 2012; Ettori et al. 2013).

The bulk and turbulence gas motions produce Doppler shifts in emission lines from heavy ions in the ICM and modify the line profiles (Inogamov & Sunyaev 2003). A line-of-sight velocity of  $1000 \text{ km s}^{-1}$  corresponds to a 22 eV shift in the 6.7 keV Fe-K line energy. Therefore the Doppler-shift measurement requires not only a high energy resolution and a good sensitivity but also a precise instrumental energy-scale calibration.

Observational efforts that used X-ray charge-coupled device (CCD) detectors with a typical energy resolution of 150 eV have constrained gas motion (for review, Ota 2012). On the basis of careful assessment of the energy scale of the X-ray Imaging Spectrometer (XIS; Koyama et al. 2007) onboard the *Suzaku* satellite (Mitsuda et al. 2007), Ota et al. (2007) placed an upper limit of  $1400 \text{ km s}^{-1}$  on bulk motions in the Centaurus cluster and suggested that the cluster mass estimated under the hydrostatic assumption is justified within a factor of 2–3. Similar measurements that used XIS data have been conducted in several nearby clusters: the upper limit on the bulk motion was derived for the Ophiuchus cluster, AWM7, A2319, the Coma cluster, and A3627 (Fujita et al. 2008; Sato et al. 2008; Sugawara et al. 2009; Sato et al. 2011; Nishino et al. 2012), and possible detection of gas bulk flow in Centaurus and A576 was reported by *Chandra* (Dupke et al. 2007; Dupke & Bregman 2006). Thus far, bulk motions has been properly detected in only one cluster: a large radial velocity of a subcluster region relative to the main cluster,  $1500 \text{ km s}^{-1}$ , was found in A2256 by *Suzaku* (Tamura et al. 2011). They suggested that the gas and galaxies are moving together in the cluster potential as a single subcluster. Doppler line broadening has been measured by the Reflection Grating Spectrometer on *XMM-Newton*, and Sanders et al. (2010) obtained a strong upper limit on the turbulent motion ( $< 200 \text{ km s}^{-1}$ ) in several objects. Pinto et al. (2015) measured the turbulent line broadening for the RGS cluster sample and reported that upper limits generally range between  $200 - 600 \text{ km s}^{-1}$  in the  $0'.8$  and  $3'.4$  core regions.

These previous studies demonstrated that the *Suzaku*/XIS spectroscopy enables meaningful constraints to be placed on bulk velocity distribution and is complementary to the turbulence measurements by the gratings, which can be performed only at the innermost region. The number of sample, however, is still insufficient for clarifying the detailed velocity structure of the ICM and for understanding the role of kinetic gas motion in the precise cluster mass estimation. In this study, we perform a systematic search for gas bulk motion in nearby clusters by utilizing the *Suzaku* archive data. The sample includes eight clusters in the nearby universe that have a wide range of X-ray morphology. We aim to constrain the presence of gas

bulk motions and to determine the dynamical state of clusters by comparing the velocity structure of the ICM with that of member galaxies in the optical band. This study provides an important pilot survey prior to the *ASTRO-H* mission (Takahashi et al. 2014) because it ranks the investigation of turbulent and macroscopic gas motions as main objectives of high-resolution spectroscopy (Mitsuda et al. 2014).

Throughout this study, we adopt  $\Omega_M = 0.27$ ,  $\Omega_\Lambda = 0.73$ , and  $H_0 = 70 \text{ km s}^{-1} \text{ Mpc}^{-1}$ . The quoted statistical errors refer to the 68% confidence ranges, unless stated otherwise.

## 2 Observation and data reduction

To investigate the ICM velocity structure and its possible relationship with the X-ray morphology, the sample was selected to include clusters with cool cores, cold fronts, and subcluster mergers. The observational features of individual clusters will be mentioned in detail in §4.1. Because a measurement of the Doppler shift of the Fe-K emission line requires a good photon statistics, the sample was limited to nearby objects with the 2–10 keV X-ray flux  $\gtrsim 10^{-11} \text{ erg s}^{-1} \text{ cm}^{-2}$  within the *Suzaku* data archive. As shown in Table 1, the sample consists of eight nearby clusters including the Centaurus and Perseus clusters, A2199, A3667, A133, A2029, A2255, and A2142. The redshift values of the target clusters,  $z_{\text{cl}}$ , were cited from the NASA/IPAC Extragalactic Database, except for the Centaurus cluster ( $z = 0.0104$ ; Dickens et al. 1986) and A2142 ( $z = 0.0909$ ; Owers et al. 2011).

We utilised X-ray spectral data obtained with XIS onboard the *Suzaku* satellite because it has an excellent sensitivity at the Fe-K line energies and the lowest background. The XIS consists of four X-ray CCD cameras including three front-illuminated (FI) CCDs (XIS-0, XIS-2<sup>1</sup>, XIS-3) and one back-illuminated (BI) CCD (XIS-1). The XIS was operated in normal modes during the observations. The details of the observations are given in Table 1, and the XIS images are shown in Fig. 1.

Data reduction was performed by using HEASOFT version 6.16, together with the calibration database released on October 1, 2014. We extracted light curves to confirm that the count rates are constant within the photon statistics. As we will detail in §3, spectral analysis was performed in two types of energy ranges including 0.7–10 keV and 5–10 keV. For the 0.7–10 keV band, the background was estimated from the blank-sky data obtained during the Lockman Hole observations, whereas the background for the 5–10 keV band is dominated by an instrumental non-X-ray background and was thus calculated using the *xisnxbgen* tool in the HEASOFT package. The energy response files were generated by using *xisrmfgen*, and the auxiliary response files were calculated using *xissimarfgen* (Ishisaki et al. 2007), in which the X-ray surface brightness

<sup>1</sup> XIS-2 is not operational as of November 2006.

**Table 1.** Log of Suzaku observations of eight clusters

Pointing	Obsid	Date	$z_{cl}$	RA (deg)	Dec (deg)	Exp <sup>a</sup> (ks)	BM <sup>b</sup>	kpc/1'
Centaurus Center	800014010	2005 Dec 27	0.0104	192.2012	−41.3132	35.8	I–II	13
Centaurus S	800015010	2005 Dec 28	–	192.2015	−41.4461	42.6	–	–
Centaurus N	800016010	2005 Dec 29	–	192.2009	−41.1804	42.0	–	–
Cen45	802008010	2007 Dec 24	–	192.5119	−41.3865	57.5	–	–
Perseus	101012010	2006 Aug 29	0.0183	49.9436	41.5175	48.8	II–III	22
A2199 Center	801056010	2006 Oct 01	0.0302	247.1922	39.4840	25.1	I	36
A2199 SE	801057010	2006 Oct 01	–	247.4695	38.9998	23.7	–	–
A2199 SW	801058010	2006 Oct 03	–	247.0222	38.9947	22.4	–	–
A2199 NW	801059010	2006 Oct 04	–	246.6242	39.5648	24.7	–	–
A2199 NE	801060010	2006 Oct 04	–	247.7662	39.3698	24.3	–	–
A3667 Center	801096010	2006 May 06	0.0556	303.1410	−56.7974	20.6	I–II	65
A3667 NW 1	801095010	2006 May 06	–	302.8177	−56.5600	17.1	–	–
A3667 NW 2	801095020	2006 Oct 30	–	302.8690	−56.6666	11.5	–	–
A3667 SE	805036010	2010 Apr 12	–	303.4605	−57.0338	64.2	–	–
A133 W	805019010	2010 Jun 07	0.0566	15.4513	−21.8877	48.5	–	66
A133 N	805020010	2010 Jun 05	–	15.6732	−21.6726	49.0	–	–
A133 E	805021010	2010 Jun 09	–	15.9075	−21.8935	50.8	–	–
A133 S	805022010	2010 Jun 08	–	15.6819	−22.1029	50.2	–	–
A2029 Center	804024010	2010 Jan 28	0.0773	227.7409	5.7498	7.6	I	88
A2029 N	804024020	2010 Jan 28	–	227.8527	6.0108	25.1	–	–
A2029 S	804024030	2010 Jan 28	–	227.6311	5.4874	17.3	–	–
A2029 E	804024040	2010 Jan 29	–	228.0053	5.6496	24.9	–	–
A2029 W	804024050	2010 Jan 30	–	227.4808	5.8608	21.4	–	–
A2255 Center	804041010	2010 Feb 07	0.0806	258.2484	64.1467	44.0	II–III	91
A2255 NW	808039010	2013 Nov 17	–	258.0206	64.3236	42.3	–	–
A2142	801055010	2007 Jan 04	0.0909	239.5312	27.2879	50.8	II	102

<sup>a</sup> Net exposure time of the XIS sensors after data filtering. <sup>b</sup> Bautz-Morgan type (Bautz & Morgan 1970).

of each cluster was modeled by the  $\beta$ -model (Mohr et al. 1999; Lieu et al. 2006).

The corners of the XIS CCD cameras illuminated by  $^{55}\text{Fe}$  calibration sources, as well as circular regions with radius  $1'$  centered on point sources detected in the *XMM-Newton* images were excluded from spectral integration regions. Here the *XMM-Newton* MOS data were reduced through the standard manner by using Science Analysis System (SAS) version 13.0.0. The event files were created by using the `emchain` tool in the SAS package. We confirmed that the contribution from the point sources was negligible in our Fe-line analysis by changing the extraction radii between  $0' - 1'.5$ .

### 3 Spectral analysis and results

To study the dynamical state of ICM, we measured the redshift of Fe-K emission lines for eight clusters of galaxies. The definition of spectral regions is described in §3.1. The method and results of spectral fitting are shown in §3.2. Because the accurate calibration of the energy scale is critical for the present purpose, we estimated the systematic error associated with the spectral analysis in §3.3 and constrained the velocity of ICM bulk motions in §3.4.

#### 3.1 Definition of spectral regions

The analysis consisted of two steps: (i) We first measured the redshift of the Fe-K lines,  $z$ , by using X-ray spectra accumulated from the entire  $18' \times 18'$  XIS field of view (FOV) to infer the mean radial velocity of the ICM. (ii) We further divided the FOV into smaller cells to constrain the spatial velocity distribution if the cluster emission was bright enough to obtain sufficient photon statistics in each cell. Although the actual physical scales of the cells may differ depending on the distance to the object, we hereafter refer to the above two cases simply as (i) the large-scale ( $18'$ ) and (ii) the small-scale ( $4'.5 - 9'.0$ ) velocity measurements.

For (i) the large-scale velocity measurements, we defined the spectral regions by the size of the XIS FOV. For five clusters (Centaurus, A2199, A3667, A133, and A2029), the spectra were extracted from each FOV of multiple pointing data as shown in Fig. 1. For the remaining clusters (Perseus, A2255, and A2142), only the central pointing data were used. Note that for the north region of A3667, spectra from a common area of two datasets (A3667 NW1 and NW2) were analyzed and are referred to as A3667 NW. For the multiple pointing data, the region identification numbers designated in Table 3 are shown in Fig. 1.

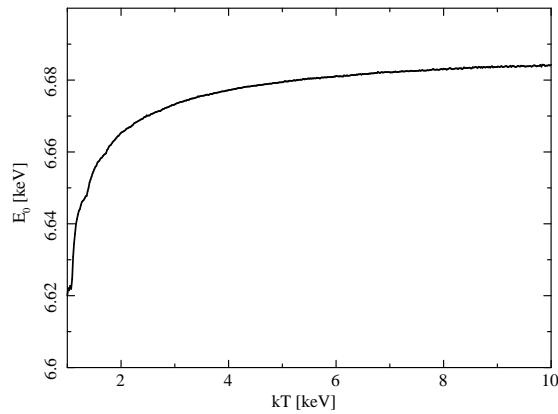


**Fig. 3.** Centroid energy of the He-like Fe-K line complex in the rest frame with  $E_0$  (keV) as a function of gas temperature,  $kT$  (keV).  $E_0$  was calculated by assuming the APEC model and the XIS energy resolution of 150 eV FWHM.

For (ii) the small-scale measurements, we divided the XIS FOVs into smaller cells. The cell sizes were chosen so that the Fe-K line spectrum contained at least 100 photons except for some very faint areas near the edge of the XIS cameras. This allows a redshift determination to the accuracy better than 10% in majority of cells. As shown in Fig. 2, XIS spectra were extracted from  $4 \times 4$  cells (i.e., 1 cell =  $4'.5 \times 4'.5$ ) in Perseus, A2199, A3667, and A2142, and  $2 \times 2$  cells (i.e., 1 cell =  $9' \times 9'$ ) in A2029 and A2255. Note that we show fitting results for all the cells in the table and figures, but exclude the faint areas near the CCD edge for which only loose constraint is obtained when we estimate the upper limits on bulk velocity.

### 3.2 Redshift determination by spectral fitting

The redshift of the Fe-K line was calculated from the relation  $z = (E_0 - E_{\text{obs}})/E_{\text{obs}}$ , where  $E_0$  and  $E_{\text{obs}}$  are the centroid energies of the He-like Fe-K line complex in the rest frame and the observed frame, respectively. Fig. 3 shows the centroid energy  $E_0$  expected in the case such that the He-like Fe-K line complex is convolved with the XIS energy resolution at a full width at half maximum (FWHM) of 150 eV at 6.7 keV. To be strict, because  $E_0$  changes with gas temperature, both  $E_0$  and  $E_{\text{obs}}$  are required to determine  $z$  in each cluster region.

To quantify the rest-frame line energy  $E_0$ , the mean gas temperature was determined by simultaneously fitting the XIS FI and BI spectra of the central pointing of each cluster in the 0.7–10 keV band to the Astrophysical Plasma Emission Code (APEC) model (Smith et al. 2001). Note that for A133, the spectra taken from A133 W was used and for the Centaurus cluster, the Cen45 subcluster was also analyzed. The temperature, metal abundance, and the normalization factor were allowed to vary, whereas the Galactic hydrogen column density,  $N_{\text{H}}$ , was fixed to a value from the Leiden/Argentine/Bonn survey (Kalberla et al. 2005). The results of the APEC model

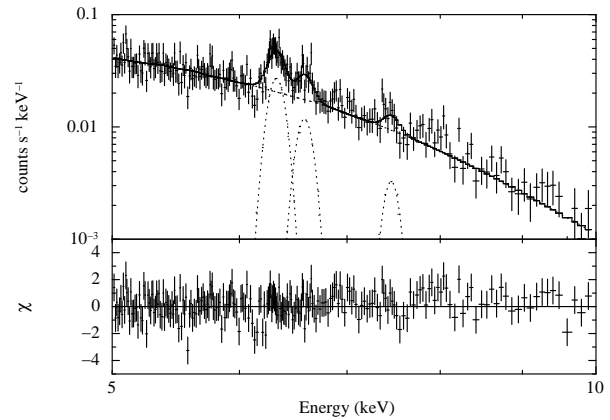


**Fig. 4.** Example of Gaussian fitting to the Fe-K line spectra. In the upper panel, the crosses show the XIS spectrum observed in A3667 cell No. 6. The solid line represents the best-fit model and the three Gaussian lines are indicated with dashed lines. In the bottom panel, the residuals of fit are shown.

fitting and  $E_0$  are shown in Table 2. Because the single-component APEC model did not give a sufficient fit to the spectra of Centaurus (e.g., Ikebe et al. 1999; Sakuma et al. 2011) and Perseus (e.g., Tamura et al. 2009), two-component APEC models were applied to these two clusters. The parameters of the hotter component are shown in Table 2.

To accurately measure the line centroid  $E_{\text{obs}}$  for the cases (i) and (ii), the XIS spectra were analyzed in the following manner, which is the same as that reported by Ota et al. (2007). The 5–10 keV spectra were fitted to a model consisting of continuum emission represented by the APEC model with a metallicity of  $Z = 0$  solar and three Gaussian lines for He-like Fe K line complex, H-like Fe K $\alpha$ , and a blend of He-like Ni K $\alpha$  and He-like Fe K $\beta$  lines. The gas temperature of the APEC model and  $E_0$  were fixed to the mean values derived above. The Gaussian width was assumed to be 0 because the intrinsic line width is smaller than the instrumental energy resolution and it does not affect the present analysis. Figure 4 shows an example of the spectral fitting. For A2255 cell No. 4, spectra from a common area of two data sets were co-added because they gave statistically consistent fitting results:  $z = 0.0720 \pm 0.0037$  (A2255 C) and  $z = 0.0743 \pm 0.0026$  (A2255 NW).

The XIS spectral bins in each cluster region were grouped so that each spectral bin contains more than 20 photons and the chi-squared fitting was performed by XSPEC version 12.8.0. The right panels in Figures 1 and 2 show the ICM redshift values obtained from the spectral fitting for (i) and (ii), respectively.

### 3.3 Systematic error of the Fe line centroid energy

To estimate the systematic error of the iron line energy, we checked the centroid energies of the Mn-K lines from the build-in calibration sources that illuminates two corners of each XIS chip. We extracted spectra of the calibration sources and fitted

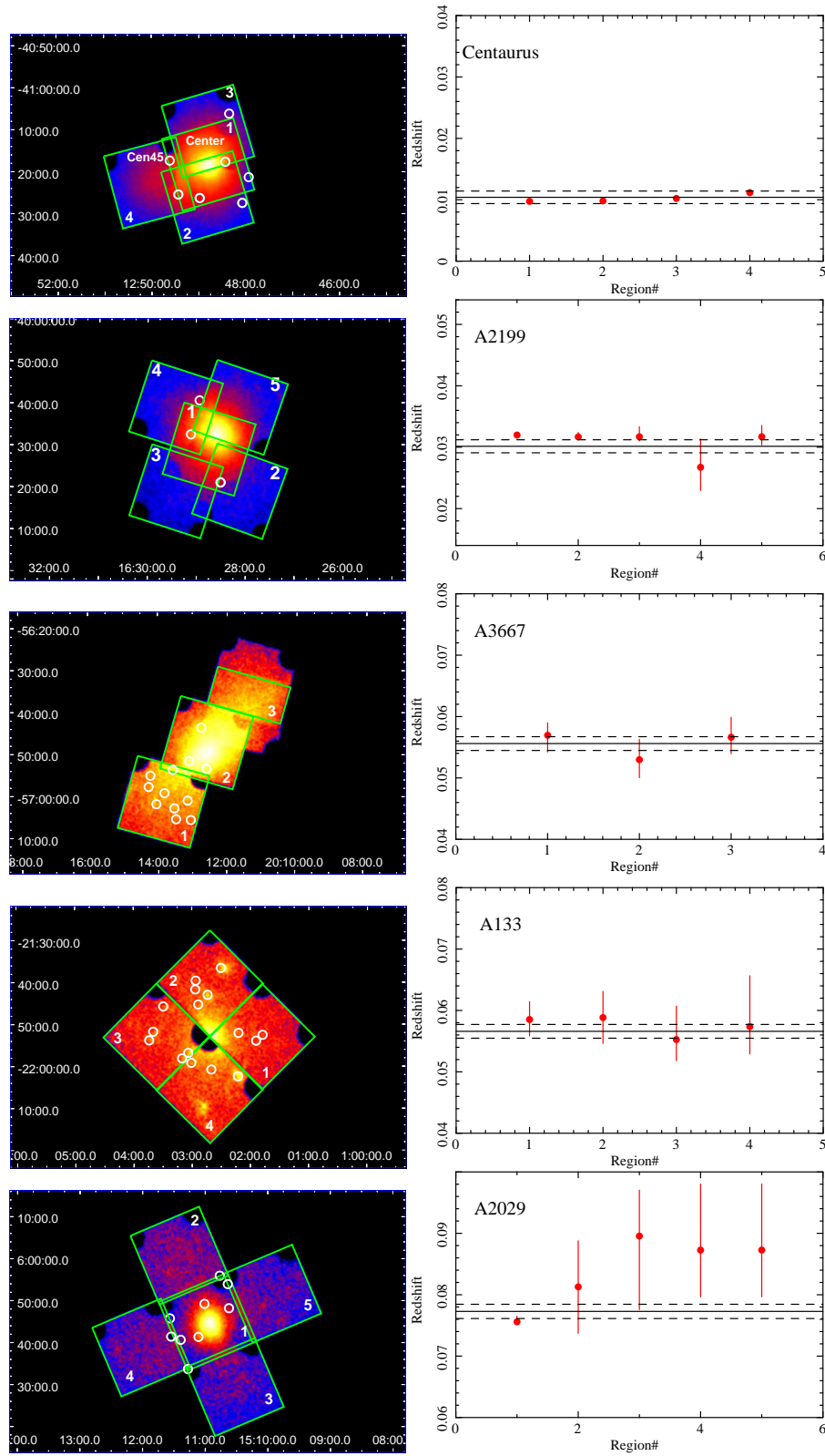


**Fig. 1.** (left) XIS-1 images in the 0.5–10 keV band, and (right) results of (i) the large-scale redshift measurements. From top to bottom, Centaurus, A2199, A3667, A133, and A2029 are displayed. In the left panels, the XIS images are smoothed by Gaussian  $\sigma = 16''$  but were not corrected for exposure and telescope vignetting. The two corners of the CCD chip illuminated by the calibration sources are excluded from the image. The spectral integration regions (i.e., the full XIS field of views of pointed observations) are shown by the green boxes and the locations of the point sources excluded from the spectral regions are marked with white circles. In the right panels, the red circles and the error bars indicate the best-fit redshift values and  $1\sigma$  statistical uncertainties. The horizontal solid lines show the optical redshift of the cluster, and the dashed lines indicate the interval of  $1\sigma$  systematic error ( $\pm 0.1\%$ ).



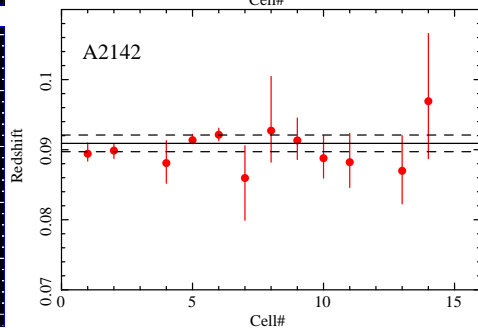
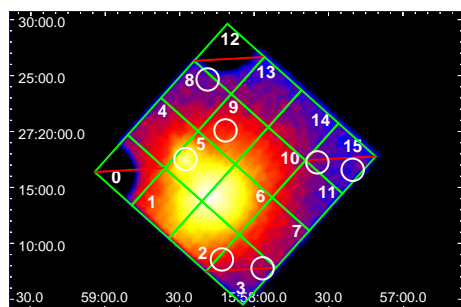
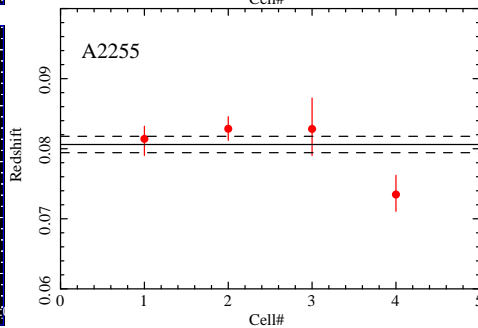
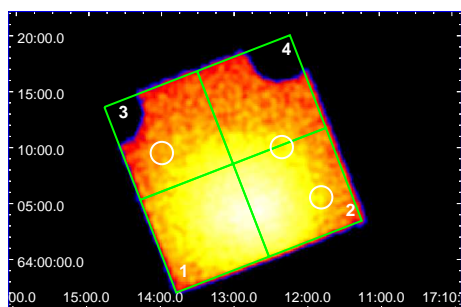
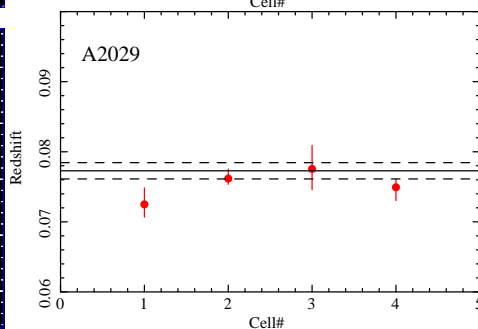
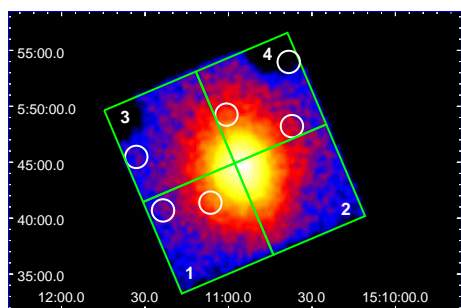
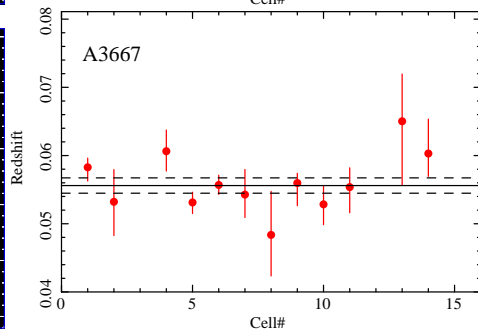
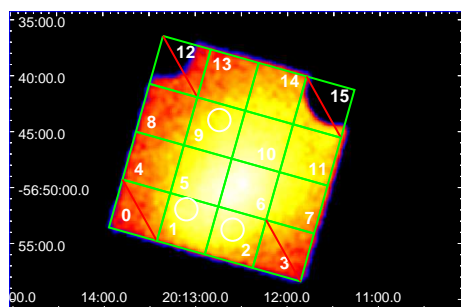
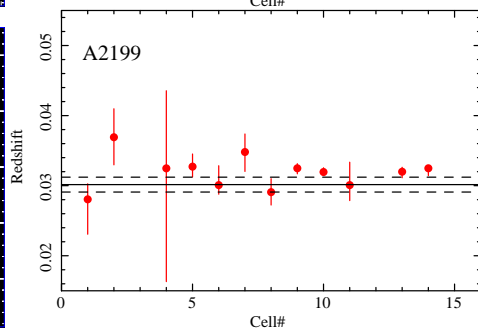
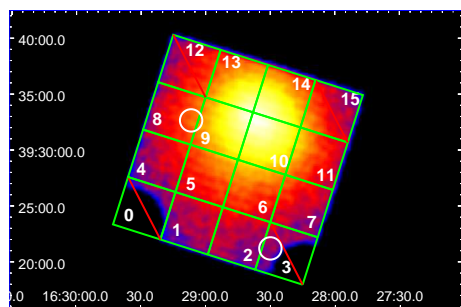
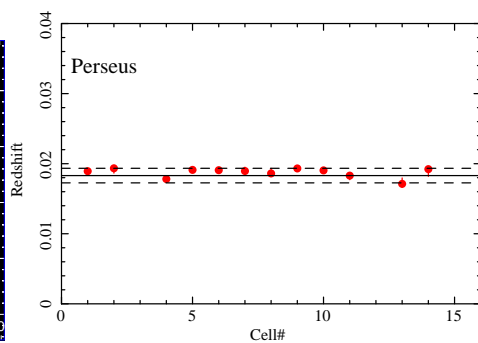
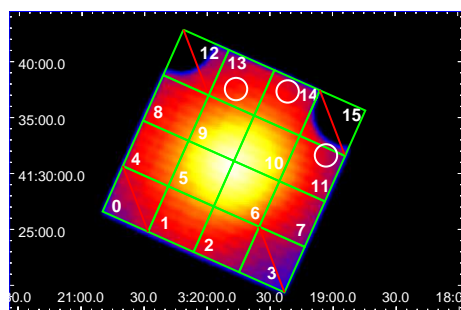


**Table 2.** Results of APEC model fitting to the XIS spectra

Pointing	$N_{\mathrm{H}}^{\mathrm{a}}$	$kT$ (keV)	$Z$ (solar) <sup>b</sup>	$z$ ( $10^{-2}$ )	$F_{\mathrm{X}}^{\mathrm{c}}$	$\chi^2/\mathrm{d.o.f.}$	$E_0$ (keV) <sup>d</sup>
Centaurus C	8.56	$3.85 \pm 0.02$	$0.417 \pm 0.007$	$0.98 \pm 0.02$	7.48	5321/5196	6.677
Cen45	8.56	$4.12 \pm 0.02$	$0.315 \pm 0.008$	$1.17 \pm 0.06$	2.36	3760/3721	6.677
Perseus	13.9	$5.68 \pm 0.01$	$0.319 \pm 0.003$	$1.913 \pm 0.003$	51.1	9216/8385	6.681
A2199 C	0.89	$4.06 \pm 0.01$	$0.347 \pm 0.006$	$3.31 \pm 0.01$	6.24	5446/5317	6.677
A3667 C	4.46	$6.73 \pm 0.05$	$0.278 \pm 0.010$	$5.54 \pm 0.06$	5.60	4774/4751	6.682
A133 W	1.59	$3.27 \pm 0.12$	$0.313 \pm 0.050$	$5.70 \pm 0.51$	0.11	365/305	6.675
A2029 C	3.26	$7.50 \pm 0.09$	$0.388 \pm 0.016$	$7.60 \pm 0.08$	8.56	2732/2728	6.683
A2255 C	2.59	$5.88 \pm 0.07$	$0.182 \pm 0.012$	$8.04 \pm 0.06$	1.46	2821/2863	6.681
A2142	3.78	$8.04 \pm 0.07$	$0.235 \pm 0.010$	$9.03 \pm 0.05$	6.50	5574/5504	6.683

<sup>a</sup> The Galactic hydrogen column density ( $10^{20} \mathrm{cm}^{-2}$ ). <sup>b</sup> The metal abundance of the ICM (solar). The abundance table in Anders & Grevesse (1989) was assumed. <sup>c</sup> The X-ray flux in the 2–10 keV band ( $10^{-11} \mathrm{ergs}^{-1} \mathrm{cm}^{-2}$ ) for each XIS pointing. <sup>d</sup> The centroid energy of the He-like Fe-K line complex in the rest frame (§3.2).

the 4–8 keV spectra with two Gaussians for the Mn K $\alpha$  and K $\beta$  along with the bremsstrahlung continuum component. The resultant line centroid of Mn K $\alpha$  line agreed with the expected value of 5.894 keV within  $\pm 0.1\%$ . This result is consistent with that reported by Ozawa et al. (2009), who performed a precise in-orbit calibration of the XIS energy-scale by using the build-in calibration sources and 1E0102.2–7219. We thus assigned  $\pm 0.1\%$  to the  $1\sigma$  systematic error on the XIS energy scale and calculated the  $1\sigma$  systematic uncertainty of the redshift ( $\sigma_{z,\mathrm{sys}}$ ) and line-of-sight velocity ( $\sigma_{v,\mathrm{sys}}$ ). The values for the sample clusters, shown in Tables 3–4, were typically  $\sigma_{z,\mathrm{sys}} = 0.001$  and  $\sigma_{v,\mathrm{sys}} = 300 \mathrm{km s}^{-1}$  for  $z = 0.01$ .

### 3.4 Constraints on the gas bulk velocity

Figure 1 shows that the ICM redshifts obtained in the case of (i) the large-scale measurements. For the eight clusters the fitted redshifts agree with the optical values ( $z_{\mathrm{cl}}$ ) within the systematic errors. As shown in Fig. 2, in case of (ii) the small-scale analyses, the redshifts in Perseus and A2142 were consistent with  $z_{\mathrm{cl}}$  within the systematic errors. On the contrary, some cells in A2199, A3667, A2029, and A2255, showed a shift of  $\Delta z = (z - z_{\mathrm{cl}})$  in excess of the  $1\sigma$  systematic error range.

The line-of-sight bulk velocity (i.e., the radial velocity relative to the optical cluster redshift) in each spectral region was calculated by  $\Delta v = c\Delta z$  and shown in Tables 3 and 4. The above results indicate that significant bulk motions exist in some cells in the cluster center. If both statistical and systematic errors are considered, the significance of the bulk velocity is  $1.6 - 1.8\sigma$  for A2199 cell Nos. 2, 7, 9, and 14,  $1.6\sigma$  for A3667 cell No. 4,  $2.1\sigma$  for A2029 cell No. 1, and  $2.6\sigma$  for A2255 cell No. 4, respectively. Here the standard deviation  $\sigma$  is given by a quadrature sum of the  $1\sigma$  statistical and systematic errors,  $\sigma_{\mathrm{tot}} = (\sigma_{z,\mathrm{stat}}^2 + \sigma_{z,\mathrm{sys}}^2)^{1/2}$ .

Table 5 gives the summary of redshift and radial velocity of gas bulk motion for cells with  $\gtrsim 2\sigma$  significance: A2029 cell No. 2 and A2255 cell No. 4. For reference, the values for cells without any significant motion, A2029 cell No. 3 and A2255

cell No. 1, are also listed. Figure 5 shows the XIS spectra of the Fe-K line emission from these objects.

As shown in Table 5 and Figure 5, we found that the ICM in the Cen45 subcluster has a redshift consistent with that of the main cluster  $z_{\mathrm{cl}} = 0.0104$  but is different from that of the subcluster in the optical band  $z_{\mathrm{sub}} = 0.0155$  at the  $3.9\sigma$  significance. The origin of the redshift difference is discussed in §4.1.1.

## 4 Discussion

On the basis of the *Suzaku*/XIS spectral analysis and careful assessment of the systematic error of the energy scale, we measured the Doppler shift of He-like Fe-K line emission to search for the ICM bulk motion in the central regions of eight nearby clusters. A signature of gas bulk motion on the order of  $1000 - 2000 \mathrm{km s}^{-1}$  was discovered in A2029 and A2255. On the contrary, no significant bulk motion was detected in five clusters. In §4.1, we compare the velocity distributions of ICM measured in §3 with those of member galaxies for individual clusters to infer the dynamical evolution of clusters. In §4.2, we discuss the impact of ICM bulk motion on the estimation of cluster gravitational mass under the assumption of hydrostatic equilibrium.

### 4.1 Velocity structures of gas and galaxies in individual clusters

#### 4.1.1 The Centaurus cluster

Optical observations of the Centaurus cluster show that this cluster has a bimodal velocity distribution of galaxies: one is associated with the main cluster centered on NGC 4696, and the other with the Cen45 subcluster centered on NGC 4709 (Lucey et al. 1986). The Cen45 subcluster has a large velocity difference of  $+1500 \mathrm{km s}^{-1}$  relative to the main cluster. Previous ASCA observations show a temperature excess in the subcluster region (Furusho et al. 2001).

The present analysis using the latest XIS energy response

**Table 3.** Results of (i) the large-scale redshift and velocity measurements

Pointing	Reg <sup>a</sup>	$z_{cl}$ ( $10^{-2}$ )	$z$ ( $10^{-2}$ )	$\sigma_{z,stat}$ ( $10^{-2}$ )	$\sigma_{z,sys}$ ( $10^{-2}$ )	$\Delta z / \sigma_{z,tot}$ <sup>b</sup>	$\Delta v$ ( $\text{km s}^{-1}$ )	$\sigma_{v,stat}$ ( $\text{km s}^{-1}$ )	$\sigma_{v,sys}$ ( $\text{km s}^{-1}$ )	$ \Delta v $ <sup>c</sup> ( $\text{km s}^{-1}$ )	$\chi^2/\text{d.o.f.}$
Centaurus C	1	1.04	0.975	0.007	0.10	-0.64	-196	20	303	< 500	1083 / 1037
Centaurus S	2	1.04	0.982	0.021	0.10	-0.56	-175	62	303	< 484	1052 / 986
Centaurus N	3	1.04	1.022	0.020	0.10	-0.18	-54	59	303	< 363	1061 / 972
Cen45	4	1.04	1.116	0.045	0.10	+0.68	+227	134	303	< 558	812 / 832
Perseus	-	1.83	1.931	0.006	0.10	+0.99	+304	19	305	< 610	2046 / 1363
A2199 C	1	3.02	3.20	0.03	0.10	+1.67	+535	86	309	< 856	758 / 774
A2199 SE	2	3.02	3.17	0.05	0.10	+1.28	+444	157	309	< 791	505 / 498
A2199 SW	3	3.02	3.17	0.12	0.10	+0.97	+450	348	309	< 916	344 / 331
A2199 NW	4	3.02	2.67	0.42	0.10	-0.80	-1042	1257	309	< 2336	224 / 232
A2199 NE	5	3.02	3.17	0.16	0.10	+0.80	+452	474	309	< 1018	250 / 251
A3667 NW	1	5.56	5.70	0.24	0.11	+0.52	+405	711	317	< 1184	337 / 320
A3667 C	2	5.56	5.30	0.31	0.11	-0.80	-791	936	317	< 1778	210 / 185
A3667 SE	3	5.56	5.66	0.30	0.11	+0.33	+309	894	317	< 1257	273 / 281
A133 W	1	5.66	5.85	0.28	0.11	+0.64	+577	839	317	< 1474	387 / 354
A133 N	2	5.66	5.88	0.42	0.11	+0.51	+672	1273	317	< 1983	336 / 370
A133 E	3	5.66	5.53	0.45	0.11	-0.29	-404	1336	317	< 1777	362 / 354
A133 S	4	5.66	5.74	0.64	0.11	+0.12	+231	1910	317	< 2167	411 / 397
A2029 C	1	7.73	7.56	0.06	0.11	-1.37	-515	189	323	< 889	368 / 342
A2029 N	2	7.73	8.13	0.75	0.11	+0.52	+1193	2260	323	< 3476	148 / 139
A2029 S	3	7.73	8.95	0.97	0.11	+1.25	+3675	2919	323	< 6612	58 / 58
A2029 E	4	7.73	8.73	0.92	0.11	+1.08	+2991	2756	323	< 5766	114 / 117
A2029 W	5	7.73	9.83	1.75	0.11	+1.20	+6302	5253	323	< 11565	70 / 70
A2255 C	-	8.06	8.19	0.10	0.11	+0.87	+394	315	324	< 846	562 / 569
A2142	-	9.09	9.10	0.05	0.11	+0.06	+21	142	327	< 378	1134 / 1105

<sup>a</sup> Region number. <sup>b</sup> Significance of the observed Doppler shift of Fe-K line, calculated by the redshift difference relative to the optical value,  $\Delta z = (z - z_{cl})$ , divided by the standard deviation  $\sigma_{tot}$  (see text). <sup>c</sup> The 68% limit on the absolute velocity difference  $|\Delta v|$ . Both statistical and systematic errors are taken into account.

yielded the redshift values for the three pointings centered on the main cluster (i.e., Centaurus cluster, Offset1, and Offset 2), which is consistent with earlier results by Ota et al. (2007). This result confirms that the bulk velocity does not largely exceed the sound velocity in the cluster core.

As shown in Table 3, the fitted redshift of Cen45 ( $0.0116 \pm 0.0005$ ) is higher than that of the center ( $0.00975 \pm 0.00007$ ); however, the difference is within the range of their systematic errors. Recently, Walker et al. (2013) confirmed the temperature excess near Cen45 on the basis of the XMM data. They modeled XMM spectra of Cen45 by superposition of two emission components from the main cluster and the Cen45 subcluster. We thus fitted the XIS spectra from a  $r = 7'$  circle centered on NGC 4709 by including their best-fit model for the  $z = 0.0104$  main cluster component in our background model to obtain the Cen45 redshift as  $0.0105 \pm 0.0011$ . Therefore the redshift difference relative to the optical subcluster is significant at the  $4\sigma$  level.

The 90% upper limit on the radial velocity of the ICM in the Cen45 subcluster was estimated as  $|\Delta v| < 760 \text{ km s}^{-1}$ . This value is twice smaller than that of the galaxies, at  $+1500 \text{ km s}^{-1}$ , suggesting the presence of an offset between the mass centroids of the ICM and galaxy distributions along the sightline. A spatial segregation between a dissipationless stellar

component and fluid-like X-ray emitting plasma has been discovered in on-going mergers such as the Bullet cluster (Clowe et al. 2006) and A2744 (Merten et al. 2011). Thus the above result supports that the Centaurus cluster has experienced a subcluster merger along the line of sight and gas near Cen45 has been heated by the strong shock (Walker et al. 2013; Churazov et al. 1999).

#### 4.1.2 The Perseus cluster

The Perseus cluster is a nearby relaxed cluster with a cool core at the center. This cluster is one of the brightest in the sky and has an intense Fe line emission. The velocity dispersion of member galaxies is approximately  $1000 \text{ km s}^{-1}$  (Kent & Sargent 1983). The XIS spectra analysis of  $4 \times 4$  cells in the center showed that the bulk velocity does not significantly exceed the sound velocity of the ICM. The 90% limit on the radial velocity is  $|\Delta v| < 830 \text{ km s}^{-1}$ , which is comparable to that obtained for the Centaurus cluster and also agrees with an in-depth analysis of *Suzaku*'s multiple pointing data (Tamura et al. 2014).

#### 4.1.3 A2199

A2199 is a nearby relaxed cluster with smooth and symmetric gas morphology. The cD galaxy hosts a radio jet and its interaction with the surrounding gas was shown by the *ROSAT* obser-



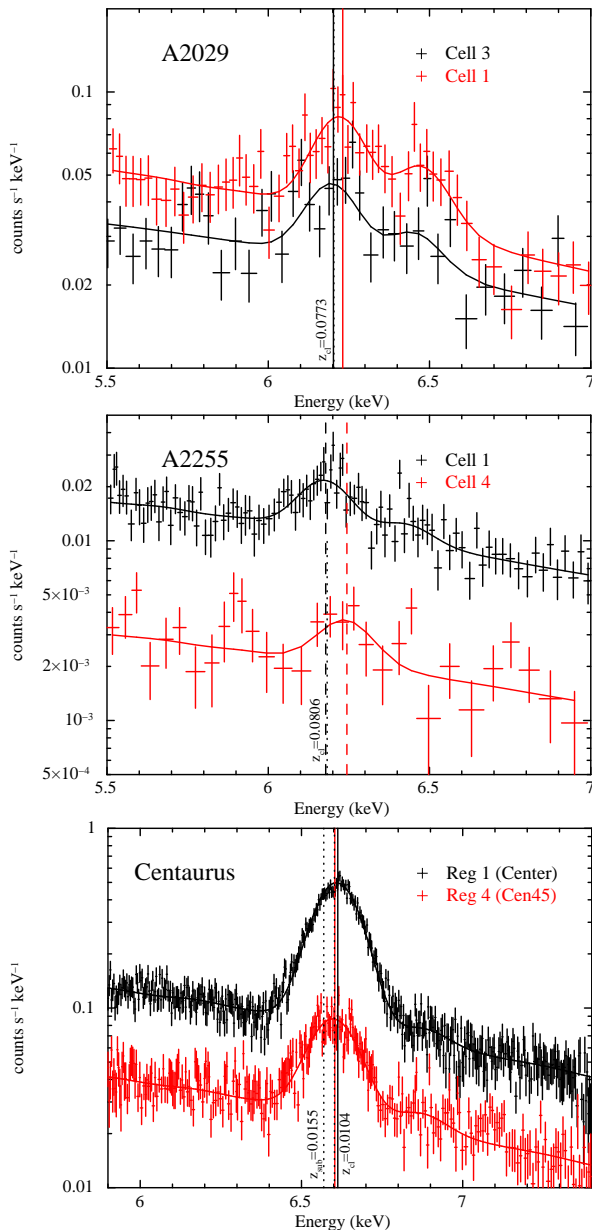


**Fig. 5.** XIS spectra of A2029 (top), and A2255 (middle), and Centaurus (bottom). In each panel, the spectra of two cells inside each cluster (crosses) and the best-fit Gaussian models (the solid curves) are shown. The best-fit centroid energies of the He-like Fe-K line complex are indicated by the vertical dashed lines. The line centroid energies expected from the cluster redshifts and that from the subcluster in Centaurus are shown by the dotted lines.

vations (Owen & Eilek 1998). Sanders & Fabian (2006) found a density jump in the cluster center, implying a Mach number  $\sim 1.5$  shock. In addition, deep *Chandra* observations showed the presence of gas sloshing due to a minor merger (Nulsen et al. 2013).

From the XIS analysis of the central region, we found a sign of large bulk velocity  $\Delta v \sim +700 - +2000 \text{ km s}^{-1}$  in cell Nos. 2, 7, 9, and 14, suggesting that the gas motion is associated with the infalling subcluster as indicated by *Chandra* data. Considering the calibration error, the significance of the detection of ICM motion is  $1.6 - 1.8\sigma$ , thus needs to be improved by follow-up observations.

#### 4.1.4 A3667

A3667 is a merging cluster with an elongated X-ray morphology. Cold fronts were detected by *Chandra* observations (Vikhlinin et al. 2001). The spatial and redshift distributions of member galaxies are bimodal (Owers et al. 2009). Their mean radial velocities are separated by  $500 \text{ km s}^{-1}$  and the maximum velocity gradient across the cluster is  $2800 \text{ km s}^{-1}$ . This cluster exhibits two radio relics and a temperature discontinuity, suggesting that A3667 has recently experienced a strong merger shock (Roettiger et al. 1999; Akamatsu et al. 2012).

The redshifts of Fe-K lines measured for A3667 Center and NW (Fig. 1, Table 3) are consistent with the optical values of  $z = 0.0555$  and  $0.0567$  for the two regions, respectively. Given the measurement uncertainties, however, the velocity difference between the two regions is not significant, resulting in 90% limit on the radial velocity  $< 2800 \text{ km s}^{-1}$  from the large-scale measurements. Although a large bulk velocity of  $+1510 \pm 960 \text{ km s}^{-1}$  is marginally detected in cell No. 4, we did not find any significant bulk motion in the cluster center (Fig. 2, Table 4), giving the 90% limit  $|\Delta v| < 3500 \text{ km s}^{-1}$  from the small-scale measurements.

#### 4.1.5 A133

A133 is an X-ray luminous cluster hosting a cD cluster and a radio relic. *Chandra* observations showed that the central cool core is irregular and extends to the northwest of the cD galaxy (Fujita et al. 2002). From *XMM* observations, a cold front was detected to the southeast of the cluster core and an upper limit to the velocity of the core relative to the rest of the cluster was estimated as  $< 230 \text{ km s}^{-1}$  in the context of the Kelvin-Helmholtz instability around the core (Fujita et al. 2004). Using a wavelet analysis of galaxy positions, Randall et al. (2010) found three distinct substructures in the cluster. They also identified a concentration of galaxies to the southwest, whose radial velocity histogram is peaked at approximately  $-1000 \text{ km s}^{-1}$ .

We did not find any significant variation in ICM velocity among the four pointing regions and placed the upper limit on the ICM radial velocity  $|\Delta v| < 3300 \text{ km s}^{-1}$  at the 90% confi-

dence level.

#### 4.1.6 A2029

A2029 is an X-ray bright, relaxed cluster, hosting a cool core at the center. A high gas temperature of 7 keV and velocity dispersion of  $1430 \text{ km s}^{-1}$  (Dressler 1979) indicate a large gravitational mass. On the basis of deep *Chandra* observations, Paterno-Mahler et al. (2013) reported that there is a spiral structure in the core region produced by sloshing motion of the ICM.

In the southeast region (cell No. 1), we detected a line-of-sight gas motion in excess of the systematic error. The analysis of *Suzaku* data yielded the velocity difference  $\Delta v = -1440 \pm 700 \text{ km s}^{-1}$ . Thus, the detection is significant at the  $2.1\sigma$  level. The measured gas velocity is likely to be larger than that expected for the sloshing motion in the cluster, at  $\sim 300 \text{ km s}^{-1}$  (Paterno-Mahler et al. 2013). The gas bulk motion will introduce a systematic uncertainty in the cluster mass, which will be discussed in the next subsection.

#### 4.1.7 A2255

A2255 is a nearby rich cluster with an elongated X-ray morphology (Burns et al. 1995). The asymmetric temperature distribution (Sakelliou & Ponman 2006) and the presence of radio halo and relics (Pizzo & de Bruyn 2009) indicate that the cluster has undergone a recent merger. In the optical, A2255 has a large velocity dispersion of  $1200 \text{ km s}^{-1}$  and several substructures approximately  $10' - 15'$  from the center. In particular, the NW and SE subclusters have a radial velocity of  $-920$  and  $+870 \text{ km s}^{-1}$ , respectively (Yuan et al. 2003), which is also indicative of mergers.

From the Gaussian fitting to the Fe-line spectra in  $2 \times 2$  cells, the redshift of the NW region (cell No. 4) was obtained as  $z = 0.073 \pm 0.003$ . This value is lower than that of optical redshift of the main cluster  $z_{\text{cl}} = 0.0806$  and is rather close to that of the NW subcluster  $0.077$ . From the XIS analysis, the velocity difference between the main cluster and NW subcluster was determined as  $|\Delta v| \sim 2100 \text{ km s}^{-1}$ , which is comparable to that of A2256 reported by Tamura et al. (2011). The present results support the idea such that the gas and galaxies are moving together as a single substructure within the cluster potential.

Considering the accuracy of the XIS energy-scale, the detection of gas motion in the NW region is at the  $2.6\sigma$  significance. A further examination, however, must await follow-up X-ray observations of subcluster regions.

#### 4.1.8 A2142

A2142 is a nearby merging cluster and is the first object in which cold fronts were identified by *Chandra* (Markevitch et al. 2000). This cluster is hot and X-ray luminous and has two cD galaxies near the center. The line-of-sight velocities of these galaxies differ by  $1600 \text{ km s}^{-1}$  (Oegerle et al. 1995), suggest-

ing that the cluster is not dynamically relaxed. Owers et al. (2011) utilized the spatial and spectral data of member galaxies to identify many group-scale substructures in A2142. Two of the subgroups denoted as S1 and S2 are located at  $1'.8$  and  $10'$  off of the cluster center. S1 is centered on the secondary cD galaxy, whereas S2 has a mean velocity of approximately  $1700 \text{ km s}^{-1}$  relative to the main cluster mass peak.

The redshifts derived from the XIS spectral analysis are consistent with the optical values within the current XIS calibration uncertainty. The S1 and S2 substructures as well as the main cluster peak are inside the XIS field of view. No significant bulk motion associated with the optical substructures was detected by *Suzaku*, giving the 90% upper limit  $|\Delta v| < 4200 \text{ km s}^{-1}$ .

### 4.2 Impact of Gas Bulk Motions on Cluster Mass Estimation

If significant bulk motions exist, a contribution of nonthermal pressure must be considered in estimating the cluster mass. Table 5 shows a comparison of the ICM bulk velocity with the sound velocity  $s = (\gamma kT / \mu m_p)^{1/2}$  in the cluster center in which the sign of bulk motions was observed. Here,  $\gamma$  is the adiabatic index and  $m_p$  is the proton mass. Their bulk velocity is marginally larger than the sound velocity.

On the basis of the *Suzaku* observations of the Centaurus cluster, Ota et al. (2007) investigated the possible impact of non-thermal pressure on the cluster mass estimate assuming simply that the gas is rotating at a circular velocity  $\sigma_r$ . The balance against the gravitational pull at a radius  $r$  is given by

$$-\frac{GM(r)\rho_{\text{gas}}}{r^2} = \frac{\partial P_{\text{gas}}}{\partial r} - \frac{f\rho_{\text{gas}}\sigma_r^2}{r} \sim \frac{\partial}{\partial r} P_{\text{gas}}(1 + f\beta_r), \quad (1)$$

$$\beta_r = \frac{\mu m_p \sigma_r^2}{kT} \sim 1.07 \left( \frac{\mu}{0.63} \right) \left( \frac{\sigma_r}{700 \text{ km s}^{-1}} \right)^2 \left( \frac{kT}{3 \text{ keV}} \right)^{-1} \quad (2)$$

where  $M(r)$  is the cluster mass interior to  $r$ ,  $\rho_{\text{gas}}$  and  $P_{\text{gas}}$  are the gas density and thermal pressure, and  $f$  is a fraction of the ICM that is rotating. Thus the total cluster mass should be higher than the hydrostatic mass by a factor of  $(1 + f\beta_r)$  because of the presence of additional pressure support.

We calculate the mass correction factor  $(1 + f\beta_r)$  assuming  $\sigma_r$  to be given by the observed  $\Delta v$  (Table 5). Following the same manner as in Tamura et al. (2014),  $f$  is approximated by the emission fraction from an interesting cell. As a result, the mass correction factor is estimated to be 1.9, 2.4 for A2029 cell No. 1, A2255 cell No. 4, respectively. Therefore, the results indicate that the nonthermal pressure support cannot be neglected in some regions of both mergers and relaxed clusters as suggested by the numerical simulations. These are, however, crude estimations and more accurate information on the spatial velocity structure is required to improve the precision of the mass determination.

The SXS microcalorimeter on board the *ASTRO-H* satellite is a non-dispersive spectrometer and enables high-resolution

(5 eV) observations in the X-ray regime (Mitsuda et al. 2014). SXS can measure the Doppler shift and broadening of iron lines caused by kinetic gas motions to an accuracy of  $100 \text{ km s}^{-1}$ , which plays an critical role in revealing the dynamics of clusters (e.g., Nagai et al. 2013; Ota 2012; Kitayama et al. 2014).

## 5 Summary

We used the *Suzaku* satellite to search for gas bulk motion in eight nearby clusters with a variety of X-ray morphologies. From the model fitting to the Fe-K line spectra, the Doppler shift was measured to high accuracy. The velocity structure of gas was compared with that of member galaxies in the optical band to study the dynamical states of clusters. This study is also important as a pilot survey for the future high-resolution spectroscopy with the X-ray microcalorimeter onboard *ASTRO-H*.

In the cores of Centaurus and Perseus, we confirmed that the bulk velocity does not largely exceed the sound velocity. For the Cen45 subcluster, we found that the upper limit on the ICM radial velocity ( $|\Delta v| < 760 \text{ km s}^{-1}$ ) is significantly smaller than that of galaxies, suggesting that there is an offset between the gas and galaxy distributions along the line of sight due to the subcluster merger.

In the cool-core cluster A2199, we found a sign of large bulk velocity, however, the significance is not sufficiently high to claim the detection. For two merging clusters with cold fronts, A2142 and A3667, and a cluster with an irregular cool core, A133, no significant gas motion was detected, yielding the 90% upper limit of  $3000 - 4000 \text{ km s}^{-1}$ .

A sign of large bulk velocity in excess of the XIS calibration uncertainty was found in the cool-core cluster A2029, and in the A2255 subcluster. We examined the impact of nonthermal pressure support in the cluster mass estimation to find it is not negligible in some regions of both relaxed and merging clusters as predicted by numerical simulations. To improve the significance of the detection, however, a further examination by follow-up observations is required.

We expect that upcoming high-resolution observations with *ASTRO-H* will determine the ICM velocity structure more accurately and will clarify the contribution of nonthermal pressure support in the cluster mass estimation.

## Acknowledgments

We are grateful to the *Suzaku* team members for satellite operation and instrumental calibration. We also thank the anonymous referee for useful comments. This was supported in part by JSPS KAKENHI grant 25400231, 25247028 (NO).

## References

Akamatsu, H., de Plaa, J., Kaastra, J., et al. 2012, *PASJ*, 64, 49

- Anders, E., & Grevesse, N. 1989, *Geochim. Cosmochim. Acta*, 53, 197
- Bautz, L. P., & Morgan, W. W. 1970, *ApJL*, 162, L149
- Burns, J. O., Roettiger, K., Pinkney, J., et al. 1995, *ApJ*, 446, 583
- Dolag, K., Vazza, F., Brunetti, G., & Tormen, G. 2005, *MNRAS*, 364, 753
- Dupke, R. A., & Bregman, J. N. 2006, *ApJ*, 639, 781
- Dupke, R. A., Mirabal, N., Bregman, J. N., & Evrard, A. E. 2007, *ApJ*, 668, 781
- Churazov, E., Gilfanov, M., Forman, W., & Jones, C. 1999, *ApJ*, 520, 105
- Clowe, D., Bradač, M., Gonzalez, A. H., et al. 2006, *ApJL*, 648, L109
- Dickens, R. J., Currie, M. J., & Lucey, J. R. 1986, *MNRAS*, 220, 679
- Dressler, A. 1979, *ApJ*, 231, 659
- Ettori, S., Donnarumma, A., Pointecouteau, E., et al. 2013, *Space Sci. Rev.*, 177, 119
- Fujita, Y., Sarazin, C. L., Kempner, J. C., et al. 2002, *ApJ*, 575, 764
- Fujita, Y., Sarazin, C. L., Reiprich, T. H., et al. 2004, *ApJ*, 616, 157
- Fujita, Y., Hayashida, K., Nagai, M., et al. 2008, *PASJ*, 60, 1133
- Furusho, T., Yamasaki, N. Y., Ohashi, T., Shibata, R., & Ezawa, H. 2001, *ApJL*, 561, L165
- Ikebe, Y., Makishima, K., Fukazawa, Y., et al. 1999, *ApJ*, 525, 58
- Inogamov, N. A., & Sunyaev, R. A. 2003, *Astronomy Letters*, 29, 791
- Ishisaki, Y., Maeda, Y., Fujimoto, R., et al. 2007, *PASJ*, 59, 113
- Kalberla, P. M. W., Burton, W. B., Hartmann, D., et al. 2005, *A&A*, 440, 775
- Kent, S. M., & Sargent, W. L. W. 1983, *AJ*, 88, 697
- Kitayama, T., Bautz, M., Markevitch, M., et al. 2014, *arXiv:1412.1176*
- Koyama, K., Tsunemi, H., Dotani, T., et al. 2007, *PASJ*, 59, 23
- Lau, E. T., Kravtsov, A. V., & Nagai, D. 2009, *ApJ*, 705, 1129
- Lieu, R., Mittaz, J. P. D., & Zhang, S.-N. 2006, *ApJ*, 648, 176
- Lucey, J. R., Currie, M. J., & Dickens, R. J. 1986, *MNRAS*, 222, 427
- Markevitch, M., Ponman, T. J., Nulsen, P. E. J., et al. 2000, *ApJ*, 541, 542
- Merten, J., Coe, D., Dupke, R., et al. 2011, *MNRAS*, 417, 333
- Mitsuda, K., Bautz, M., Inoue, H., et al. 2007, *PASJ*, 59, 1
- Mitsuda, K., Kelley, R. L., Akamatsu, H., et al. 2014, *Proc. SPIE*, 9144, 91442A
- Mohr, J. J., Mathiesen, B., & Evrard, A. E. 1999, *ApJ*, 517, 627
- Nagai, D., Vikhlinin, A., & Kravtsov, A. V. 2007, *ApJ*, 655, 98
- Nagai, D., Lau, E. T., Avestruz, C., Nelson, K., & Rudd, D. H. 2013, *ApJ*, 777, 137
- Nishino, S., Fukazawa, Y., & Hayashi, K. 2012, *PASJ*, 64, 16
- Norman, M. L., & Bryan, G. L. 1999, *The Radio Galaxy Messier 87*, 530, 106
- Nulsen, P. E. J., Li, Z., Forman, W. R., et al. 2013, *ApJ*, 775, 117
- Oegerle, W. R., Hill, J. M., & Fitchett, M. J. 1995, *AJ*, 110, 32
- Ota, N., Fukazawa, Y., Fabian, A. C., et al. 2007, *PASJ*, 59, 351
- Ota, N. 2012, *Research in Astronomy and Astrophysics*, 12, 973
- Owen, F. N., & Eilek, J. A. 1998, *ApJ*, 493, 73
- Owers, M. S., Couch, W. J., & Nulsen, P. E. J. 2009, *ApJ*, 693, 901
- Owers, M. S., Nulsen, P. E. J., & Couch, W. J. 2011, *ApJ*, 741, 122
- Ozawa, M., Uchiyama, H., Matsumoto, H., et al. 2009, *PASJ*, 61, 1
- Pinto, C., Sanders, J. S., Werner, N., et al. 2015, *A&A*, 575, A38
- Pizzo, R. F., & de Bruyn, A. G. 2009, *A&A*, 507, 639
- Rasia, E., Meneghetti, M., Martino, R., et al. 2012, *New Journal of Physics*, 14, 055018
- Paterno-Mahler, R., Blanton, E. L., Randall, S. W., & Clarke, T. E. 2013, *ApJ*, 773, 114
- Randall, S. W., Clarke, T. E., Nulsen, P. E. J., et al. 2010, *ApJ*, 722, 825
- Ricker, P. M., & Sarazin, C. L. 2001, *ApJ*, 561, 621
- Roettiger, K., Loken, C., & Burns, J. O. 1997, *ApJS*, 109, 307

- Roettiger, K., Burns, J. O., & Stone, J. M. 1999, *ApJ*, 518, 603
- Sakelliou, I., & Ponman, T. J. 2006, *MNRAS*, 367, 1409
- Sakuma, E., Ota, N., Sato, K., Sato, T., & Matsushita, K. 2011, *PASJ*, 63, 979
- Sanders, J. S., & Fabian, A. C. 2006, *MNRAS*, 371, L65
- Sanders, J. S., Fabian, A. C., Smith, R. K., & Peterson, J. R. 2010, *MNRAS*, 402, L11
- Sato, K., Matsushita, K., Ishisaki, Y., et al. 2008, *PASJ*, 60, 333
- Sato, T., Matsushita, K., Ota, N., et al. 2011, *PASJ*, 63, 991
- Smith, R. K., Brickhouse, N. S., Liedahl, D. A., & Raymond, J. C. 2001, *ApJL*, 556, L91
- Sugawara, C., Takizawa, M., & Nakazawa, K. 2009, *PASJ*, 61, 1293
- Takahashi, T., Mitsuda, K., Kelley, R., et al. 2014, *Proc. SPIE*, 9144, 914425
- Tamura, T., Maeda, Y., Mitsuda, K., et al. 2009, *ApJL*, 705, L62
- Tamura, T., Hayashida, K., Ueda, S., & Nagai, M. 2011, *PASJ*, 63, 1009
- Tamura, T., et al. 2014, *ApJ*, accepted
- Vikhlinin, A., Markevitch, M., & Murray, S. S. 2001, *ApJL*, 549, L47
- Walker, S. A., Fabian, A. C., & Sanders, J. S. 2013, *MNRAS*, 435, 3221
- Yuan, Q., Zhou, X., & Jiang, Z. 2003, *ApJS*, 149, 53

**Table 4.** Results of (ii) the small-scale redshift and velocity measurements

Cluster	Cell	$z_{cl}$ ( $10^{-2}$ )	$z$ ( $10^{-2}$ )	$\sigma_{z,stat}$ ( $10^{-2}$ )	$\sigma_{z,sys}$ ( $10^{-2}$ )	$\Delta z / \sigma_{z,tot}$	$\Delta v$ ( $\text{km s}^{-1}$ )	$\sigma_{v,stat}$ ( $\text{km s}^{-1}$ )	$\sigma_{v,sys}$ ( $\text{km s}^{-1}$ )	$ \Delta v $ ( $\text{km s}^{-1}$ )	$\chi^2/\text{d.o.f.}$
Perseus	1	1.83	1.89	0.010	0.10	+0.61	+188	31	305	< 495	600 / 525
	2	1.83	1.93	0.051	0.10	+0.92	+313	152	305	< 654	519 / 456
	4	1.83	1.78	0.034	0.10	-0.46	-148	101	305	< 470	526 / 524
	5	1.83	1.91	0.008	0.10	+0.80	+245	25	305	< 551	1245 / 1056
	6	1.83	1.91	0.011	0.10	+0.75	+230	32	305	< 538	1193 / 1069
	7	1.83	1.90	0.048	0.10	+0.58	+195	145	305	< 534	414 / 451
	8	1.83	1.86	0.038	0.10	+0.28	+93	113	305	< 418	382 / 433
	9	1.83	1.93	0.011	0.10	+0.99	+305	34	305	< 613	1071 / 971
	10	1.83	1.90	0.021	0.10	+0.71	+222	62	305	< 534	1095 / 1021
	11	1.83	1.83	0.044	0.10	-0.01	-2	132	305	< 335	457 / 443
	13	1.83	1.71	0.067	0.10	-0.97	-354	200	305	< 719	308 / 299
	14	1.83	1.92	0.063	0.10	+0.77	+276	188	305	< 634	433 / 387
A2199	1	3.02	2.80	0.36	0.10	-0.57	-646	1080	309	< 1769	9 / 19
	2	3.02	3.69	0.40	0.10	+1.62	+2014	1201	309	< 3253	15 / 18
	4	3.02	3.25	1.36	0.10	+0.17	+682	4085	309	< 4779	14 / 26
	5	3.02	3.27	0.16	0.10	+1.30	+755	491	309	< 1335	40 / 49
	6	3.02	3.01	0.20	0.10	-0.05	-34	610	309	< 718	42 / 52
	7	3.02	3.48	0.27	0.10	+1.61	+1381	801	309	< 2239	24 / 23
	8	3.02	2.91	0.19	0.10	-0.52	-336	564	309	< 979	25 / 29
	9	3.02	3.25	0.07	0.10	+1.82	+685	216	309	< 1062	203 / 190
	10	3.02	3.20	0.05	0.10	+1.51	+525	158	309	< 873	212 / 224
	11	3.02	3.01	0.27	0.10	-0.04	-35	821	309	< 912	45 / 43
	13	3.02	3.20	0.07	0.10	+1.41	+538	224	309	< 919	156 / 153
	14	3.02	3.25	0.07	0.10	+1.86	+686	200	309	< 1054	177 / 144
A3667	1	5.56	5.83	0.17	0.11	+1.35	+804	503	317	< 1399	73 / 69
	2	5.56	5.32	0.48	0.11	-0.48	-715	1452	317	< 2201	29 / 36
	4	5.56	6.06	0.30	0.11	+1.58	+1510	903	317	< 2467	28 / 31
	5	5.56	5.31	0.16	0.11	-1.31	-742	469	317	< 1308	100 / 138
	6	5.56	5.57	0.14	0.11	+0.05	+26	424	317	< 555	184 / 164
	7	5.56	5.43	0.35	0.11	-0.36	-397	1056	317	< 1500	44 / 36
	8	5.56	4.84	0.62	0.11	-1.15	-2169	1862	317	< 4057	43 / 24
	9	5.56	5.60	0.24	0.11	+0.14	+111	714	317	< 892	50 / 67
	10	5.56	5.28	0.29	0.11	-0.90	-826	863	317	< 1745	101 / 105
	11	5.56	5.54	0.33	0.11	-0.07	-67	987	317	< 1104	46 / 41
	13	5.56	6.50	0.81	0.11	+1.15	+2828	2444	317	< 5292	30 / 40
	14	5.56	6.03	0.42	0.11	+1.09	+1410	1259	317	< 2708	45 / 40
A2029	1	7.73	7.25	0.21	0.11	-2.05	-1443	623	323	< 2145	103 / 117
	2	7.73	7.62	0.11	0.11	-0.73	-338	328	323	< 799	209 / 182
	3	7.73	7.76	0.32	0.11	+0.08	+76	949	323	< 1078	106 / 83
	4	7.73	7.49	0.15	0.11	-1.28	-711	450	323	< 1265	134 / 119
A2255	1	8.06	8.14	0.21	0.11	+0.34	+242	625	324	< 946	199 / 247
	2	8.06	8.28	0.17	0.11	+1.12	+673	506	324	< 1275	259 / 232
	3	8.06	8.28	0.41	0.11	+0.52	+667	1231	324	< 1940	110 / 112
	4	8.06	7.35	0.26	0.11	-2.56	-2141	772	324	< 2978	128 / 136
A2142	1	9.09	8.94	0.13	0.11	-0.88	-444	386	327	< 951	304 / 292
	2	9.09	8.99	0.10	0.11	-0.69	-310	304	327	< 757	232 / 293
	4	9.09	8.81	0.30	0.11	-0.87	-843	912	327	< 1812	89 / 90
	5	9.09	9.14	0.06	0.11	+0.36	+137	192	327	< 516	451 / 485



**Table 4.** (Continued)

Cluster	Cell	$z_{\text{cl}}$ ( $10^{-2}$ )	$z$ ( $10^{-2}$ )	$\sigma_{z,\text{stat}}$ ( $10^{-2}$ )	$\sigma_{z,\text{sys}}$ ( $10^{-2}$ )	$\Delta z/\sigma_{z,\text{tot}}$	$\Delta v$ ( $\text{km s}^{-1}$ )	$\sigma_{v,\text{stat}}$ ( $\text{km s}^{-1}$ )	$\sigma_{v,\text{sys}}$ ( $\text{km s}^{-1}$ )	$ \Delta v $ ( $\text{km s}^{-1}$ )	$\chi^2/\text{d.o.f.}$
	6	9.09	9.21	0.09	0.11	+0.87	+370	269	327	< 794	504 / 557
	7	9.09	8.60	0.53	0.11	−0.91	−1482	1595	327	< 3110	76 / 72
	8	9.09	9.27	0.61	0.11	+0.29	+544	1835	327	< 2408	40 / 44
	9	9.09	9.13	0.30	0.11	+0.13	+126	887	327	< 1071	118 / 101
	10	9.09	8.88	0.30	0.11	−0.66	−634	908	327	< 1599	125 / 134
	11	9.09	8.82	0.39	0.11	−0.67	−806	1158	327	< 2010	45 / 47
	13	9.09	8.70	0.49	0.11	−0.79	−1175	1460	327	< 2670	38 / 44
	14	9.09	9.69	0.89	0.11	+0.67	+1805	2677	327	< 4502	41 / 46

**Table 5.** ICM redshift and the radial velocity of gas bulk motion

Cluster	Cell	$z_{\text{cl}}$ ( $10^{-2}$ )	$z$ ( $10^{-2}$ )	$ \Delta z/\sigma_{z,\text{tot}} ^{\text{a}}$ ( $\text{km s}^{-1}$ )	$\Delta v$ ( $\text{km s}^{-1}$ )	$s^{\text{b}}$
A2029	1	7.73	$7.25 \pm 0.23$	2.1	$-1443 \pm 702$	1403
	3 <sup>c</sup>	7.73	$7.76 \pm 0.33$	0.1	$76 \pm 1002$	1403
A2255	4	8.06	$7.35 \pm 0.28$	2.6	$-2141 \pm 837$	1248
	1 <sup>c</sup>	8.06	$8.14 \pm 0.23$	0.3	$242 \pm 704$	1248
Cen45	4	1.04	$1.12 \pm 0.11$	0.7	$+227 \pm 332$	880
	4	1.55 <sup>d</sup>	$1.12 \pm 0.11$	3.9	$-1303 \pm 332$	880

The  $1\sigma$  errors including the statistical and systematic uncertainties are quoted. <sup>a</sup> Significance of the redshift difference,  $\Delta z$ , from the XIS spectral fit divided by the standard deviation including the statistical and systematic uncertainties. <sup>b</sup> Sound velocity of the ICM (see §4.2). <sup>c</sup> Reference cell. <sup>d</sup> The optical redshift of the Cen45 subcluster.